A camera for coherent diffractive imaging and holography with a soft-X-ray free electron laser

Saša Bajt,[1,a *] Henry N. Chapman,[1,b] Eberhard A. Spiller[2], Jennifer B. Alameda[1], Bruce W. Woods[1], Matthias Frank[1], Michael J. Bogan[1], Anton Barty[1], Sebastien Boutet[3,4], Stefano Marchesini[5], Stefan P. Hau-Riege[1], Janos Hajdu[3,4], David Shapiro[5]

[1]Physics and Advanced Technologies, Lawrence Livermore National Laboratory, 7000 East Avenue, Livermore, CA 94550, USA

[2]Spiller X-ray Optics, Livermore, CA 94550, USA

[3]Stanford Synchrotron Radiation Laboratory, Stanford Linear Accelerator Center, 2575 Sand Hill Road, Menlo Park, CA 94305, USA.

[4]Laboratory of Molecular Biophysics, Department of Cell and Molecular Biology, Uppsala University, Husargatan 3, Box 596, SE-75124 Uppsala, Sweden

[5]Advanced Light Source, Lawrence Berkeley National Laboratory, 1 Cyclotron Road, Berkeley, CA 94720, USA.

[a]Current address: Deutsches Elektronen- Synchrotron, HASYLAB, Notkestraße 85, 22607 Hamburg, Germany

[b]Current address: Centre for Free-Electron Laser Science, U. Hamburg/DESY, Notkestraße 85, 22607 Hamburg, Germany

*Corresponding author: sasa.bajt@desy.de

Abstract

We describe a camera to record coherent scattering patterns with a soft-X-ray free-electron laser. The camera consists of a laterally-graded multilayer mirror which reflects the diffraction pattern onto a CCD detector. The mirror acts as a bandpass filter both for wavelength and angle, which isolates the desired scattering pattern from non-sample scattering or incoherent emission from the sample. The mirror also solves the particular problem of the extreme intensity of the FEL pulses, which are focused to greater than 10^{14} W/cm^2. The strong undiffracted pulse passes through a hole in the mirror and propagates on to a beam dump at a distance behind the instrument rather than interacting with a beamstop placed near the CCD. The camera concept is extendable for the full range of the fundamental wavelength of the FLASH FEL (i.e. between 6 nm and 60 nm) and into the water window. We have fabricated and tested various multilayer mirrors for wavelengths of 32 nm, 16 nm, 13.5 nm, and 4.5 nm. At the shorter wavelengths mirror roughness must be minimized to reduce scattering from the mirror. We have recorded over 30,000 diffraction patterns at the FLASH free-electron laser with no observable mirror damage or degradation of performance.

OCIS codes: 040.1490, 030.1670, 050.1940, 140.2600, 340.7470, 310.1210, 310.4165.

1. Introduction

The current development of fourth-generation X-ray light sources, such as the LCLS (Linac Coherent Light Source) at the Stanford Linear Accelerator Center (SLAC), the European XFEL (X-ray Free Electron Laser) in Hamburg and Japanese Spring-8 Compact SASE Source

(SCSS) has sparked many ideas for new science that will only be possible with 9 orders of magnitude higher peak X-ray brightness than what is currently available at state-of-the-art synchrotrons [1]. The properties of these sources, namely short wavelength, ultrafast pulse duration, high fluence, and spatial coherence, make them ideal for high-resolution ultrafast imaging of non-crystalline materials. At synchrotron sources, radiation damage limits the resolution achievable to image biological materials [2]. By using ultrafast X-ray pulses of 100 fs or less in duration it is possible to record structural information from a sample before radiation damage destroys it [3]. The resolution limitations of current X-ray optics [4], and also their liability to destruction by intense pulses, can be overcome by the "lensless" methods of coherent X-ray diffractive imaging [5-8] and Fourier-transform X-ray holography [9-11]. Such methods should be applicable down to scale lengths of interatomic distances with reproducible samples, such as uncrystallized macromolecules, virus particles, and protein complexes [12].

The 10–100 fs pulse duration of X-ray FELs also allows the dynamic study of transient atomic processes, such as protein function, phase transitions, and laser-matter interactions. While many experiments have been carried out in these broad areas by time-resolved X-ray diffraction of crystals, coherent diffractive imaging and holography promise to expand these techniques to more general non-crystalline systems.

In the method of diffractive imaging a coherent diffraction pattern is recorded in (or near) the far field of a sample. Unlike diffraction from a crystal, where only Bragg peaks are recorded, the diffraction pattern of a non-periodic object is continuous. This pattern is recorded on a two-dimensional pixel detector such as a CCD. A computer algorithm essentially takes the place of the lens, by determining how to recombine the scattered light to form an image. This requires the determination of the phases corresponding to the measured intensity samples, which can be

achieved by iterative methods [13,14]. Alternatively, a reference beam can be generated by a well-defined scattering structure placed near—or integrated into—the sample [11,15]. The reference beam interferes with the diffraction from the object, generating a hologram. Both of these techniques record a diffraction pattern, and require the same apparatus. For scattering patterns measured in the far field the resolution of the image is limited only by the X-ray wavelength and the largest scattering angle recorded in the diffraction pattern or hologram.

In this paper we describe a novel diffractive imaging camera that we designed and fabricated to record coherent diffraction patterns and holograms at the new short-pulse, intense, soft-X-ray source, FLASH (Free Electron LASer in Hamburg) [16] at DESY (Deutsches Elektronen Synchrotron, Hamburg, Germany). The key to this camera is the use of a laterally-graded multilayer mirror to reflect the diffracted wavefield onto a CCD detector, yet which transmits the intense undiffracted beam, through a hole, harmlessly away from the sensitive detector. We first give details about the experimental setup, and then describe the geometry of the multilayer mirror. Mirror roughness will affect the diffraction pattern, as examined in Sec. 3. We have made various mirrors for wavelengths of 32 nm, 16 nm (the FEL 2nd harmonic), 13.5 nm and 4.5 nm (3rd harmonic), which are specified in Sec. 4. The performance of the camera is illustrated with a single-pulse coherent diffraction pattern and the high-resolution image reconstructed from the pattern.

2. Experimental setup

The FLASH source produces photon pulses of energy of 100 μJ and higher, 10-25 fs duration, and is bright enough so that these pulses can be focused to peak intensities higher than 10^{15} W/cm^2. This is high enough to convert all materials placed in that beam into plasma. Hence, the samples under study are destroyed as a consequence of the imaging process.

However, the pulse duration is much shorter than the time it takes the sample to expand or be modified at the image resolution length scale, so the images represent the undamaged object [3,12].

For weakly-scattering X-rays, the diffraction pattern of a sample placed in the beam contains only a small fraction of the incident number of photons, and the undiffracted beam is approximately as intense as the incident beam. At synchrotron sources this strong undiffracted beam is usually blocked with a beamstop to prevent saturation or damage to the CCD detector. However, at FLASH, the pulse intensity would ablate the beamstop, potentially creating plasma emission radiation, scattering, and debris that could all hit the CCD. Of course the sample will also turn into a plasma, so we require a filter to prevent out-of-band radiation from the sample from obscuring the coherent diffraction signal. We solved these problems with a flat multilayer-coated mirror oriented at 45° to the beam, with a 1.2-mm diameter hole in the middle for the direct beam to pass through, shown in Fig. 1. The light scattered from the object reflects from the 45° mirror onto a bare CCD that is normal to the reflected optical axis. The multilayer period must vary across the face of the mirror to maintain the Bragg condition for the elastically-scattered radiation emanating from the sample. Since out-of-band plasma radiation emitted by the sample will not satisfy the Bragg condition it is efficiently filtered from the measured diffraction pattern. Furthermore, the mirror also filters for ray direction. Stray light, from the scattering of upstream beamline optics for example, will hit the mirror at an angle that does not obey the Bragg law, and will also be filtered out.

We carry out experiments in a vacuum chamber that is mounted to beamline BL2 at the FLASH facility. The pulses from the FEL are focused by the beamline ellipsoidal mirror to a 20-μm spot in the center of the experiment chamber. The chamber houses a motorized stage to hold

and position the sample, a motorized stage to hold and position an aperture, and the diffraction camera. The camera, consisting of the CCD and 45° mirror are integrated into one mechanical structure. This entire structure can be rotated by 30° about an axis that passes through the sample position, perpendicular to the incident beam. In this configuration the direct beam no longer passes through the hole in the mirror, but the mirror clears the direct beam. In this way we can record off-axis diffraction patterns up to a scattering angle of 45°. Note that since the mirror rotates about the sample position, the incident angles on the mirror remain the same as in the on-axis geometry.

The coating design, discussed in Sec. 3, fixes the sample to mirror distance, which must always remain the same. We can increase the sample to CCD distance (the camera length) by moving the camera further from the mirror in a direction along the reflected optic axis.

We used two versions of a Princeton Instruments model PI-MTE in-vacuum thermoelectrically-cooled back-illuminated CCD camera that is sensitive to low energy x-rays. The camera readout is digitized into a 16 bit dynamic range with a 26.8 × 26.0 mm active area. One camera had 1340 × 1300 pixels, and the other 2000 × 2000 pixels. The camera is designed to use water cooling to remove heat from the thermoelectric cooler in the camera but because of beamline restrictions we had to flow cold nitrogen gas at a high rate through the cooling lines to remove the heat.

Time-resolved single-shot X-ray imaging of photoinduced processes is carried out with a visible-light laser pump pulse synchronized with the FEL pulse. In this case, 25 mm × 25 mm filters of free-standing metal-coated parylene are placed directly in front of the CCD to block visible light from reaching the detector. Depending on the FEL wavelength we use 100 nm to 180 nm thickness of aluminum or zirconium, coated on a 100-nm thick parylene film,

manufactured by Luxel Corp. The total transmission of the 100 nm Zr filter is ~70% at 13.5 nm wavelength. We additionally use filters to increase the effective dynamic range of the measured diffraction pattern. In this case we deposit a 5 or 7 mm diameter circle of 48 nm thick Ir on the filter, by sputtering through a circular aperture. The circle transmits 13% as compared with the rest of the filter, preventing saturation of the high-intensity low-angle diffraction.

The experimental hardware is extremely flexible allowing various components to be replaced or moved in order to perform various types of experiments using different hardware configurations. One configuration allows us to illuminate particles or structures on substrates and move the sample substrates to various locations to sub micron accuracies. A 180° rotation of the entire experiment allows us to perform time-delay holography measurements [17]. The apparatus also includes a sample-viewing optical microscope, and allows for the injection of particles into the FEL beam [18], and the illumination of the sample with a polarized short-pulse laser (for ultrafast time-resolved imaging).

3. Mirror Geometry

The range of angles that must reflect from the flat mirror depends on the largest scattering angles of rays from the sample that are detected. For a largest scattering angle α the flat mirror must reflect between approximately $45°-\alpha$ to $45°+\alpha$. As in all coherent imaging schemes, the spatial resolution length, s, of the retrieved image is given by $s = \lambda/\sin \alpha$, where λ is the wavelength, and finest spatial resolution is achieved with the largest detector numerical aperture, $\sin \alpha$. In our setup this angle was limited practically to $\alpha = 14°$ by the 25-mm width of

the CCD and the shortest sample to CCD distance of 50 mm (this is in the far field for objects smaller than 10 μm and wavelengths longer than 4 nm).

The 45°±14° range of incidence angles is much larger than the angular width of multilayer reflectivity curves. Therefore the multilayer period must vary over the surface of the mirror to maintain high reflectivity at each point. The period d of a multilayer to efficiently reflect a wavelength λ at an incidence angle θ is given approximately by

$$d = \frac{\lambda}{2\sqrt{\sin^2\theta - 2\bar{\delta}}}, \tag{1}$$

where $\bar{\delta}$ is the mean real part of the refractive index decrement of the multilayer materials [19]. In practice the d spacing is optimized iteratively based on soft-X-ray reflectometry [20] measurements of trial mirrors. The geometry of the coating depends on the sample to mirror distance, l, measured along the optic axis, as shown in Fig. 1. Note that the mirror coating must be rotationally symmetric about the mirror normal that passes through the sample point. This point on the mirror surface is outside the physical mirror extents, but we refer to this as the origin, and define a radial distance r across the mirror from this origin. We see from Fig. 1 that the incidence angle is given by

$$\tan\theta = \frac{l}{\sqrt{2}\,r}. \tag{2}$$

The incidence angle for a ray along the optic axis is of course 45°, which occurs at $r = l/\sqrt{2}$. The multilayer thickness profile is thus given by

$$d(r) = \frac{\lambda}{2\sqrt{l^2/(l^2+2r^2) - 2\bar{\delta}}} \cong \frac{\lambda}{2l}\sqrt{l^2+2r^2}. \tag{3}$$

We coated mirrors for a sample to mirror distance of l = 35 mm. For an angular range of -15° to +15° this corresponds to r = 14.3 mm to r = 42.9 mm and more than a doubling of the

multilayer period over this short distance. The mirrors are circular with a diameter of 50 mm, and so the coating symmetry axis lies just at the edge of the mirror. This is outside the active area of the mirror, defined by the projected region of the CCD onto the mirror. A sector of the mirror substrate is removed (at r = 42.5 mm) to allow the mirror to be placed close to the CCD chip and reduce the sample to CCD distance. The coatings were made by magnetron sputtering, using a system described in detail elsewhere [21]. To achieve the desired period variation $d(r)$ across the optic, we used a combination of platter velocity modulation [22] and a shadow mask. The stationary mask was placed in front of two mirrors mounted together in a holder which was spun about the point $r = 0$. The thickness of the coating at a radius r increases in proportion to the time that the mask at r is open, which is simply proportional to φ, the angular coordinate of the opening. That is, we initially design the mask according to the polar coordinates $(r, \varphi) = (r, d(r)/d_0)$, where d_0 is a normalization which depends on the overall deposition rate, as shown in Fig. 2. After depositing coatings onto test wafers and measuring $d(r)$ by soft-x-ray reflectometry, a correction to the mask is calculated to achieve the desired profile.

The coating profile of Eqn. (3) allows optimal reflection for only one mirror distance l from the mirror. That means that the coordinate system must be precisely transferred between the coating system, the mirror metrology instrument, and the FEL experiment. The tolerance of this registration depends on the angular acceptance of the multilayer mirror, which generally becomes narrower as the wavelength is reduced.

It is clear that the mirror can be rotated in any direction about the source point without affecting the angles of incidence, and that the alignment has only three degrees of freedom. These degrees of freedom can be characterized by the translational errors of the sample from the ideal sample position. Rays emanating from a point displaced from the ideal sample point S

(Fig. 1) will be incident on the mirror surface at an incorrect incidence angle and will not be efficiently reflected. We define a tolerable angular misalignment, $\Delta\theta$, defined as the half width at half maximum reflectivity of the multilayer. For the geometry shown in Fig. 1, the tolerable sample displacements will be given by

$$\Delta x = \pm \frac{l\,\Delta\theta}{\sqrt{2}\sin\theta} \tag{4}$$

$$\Delta y = \pm \frac{l\,\Delta\theta}{\sqrt{2}\sin\theta}\frac{1}{\cos(\frac{\pi}{4}-\theta)} \tag{5}$$

$$\Delta z = \pm \frac{l\,\Delta\theta}{\sqrt{2}\sin\theta}\frac{1}{\sin(\frac{\pi}{4}-\theta)} \tag{6}$$

For any displacement from *S*, the incidence angle error will be greatest for points on the mirror closest to *S*, which are those of highest incidence angle, $\theta = 60°$. These incidence angles also have the narrowest (that is, most stringent) multilayer acceptance width $\Delta\theta$. We usually characterize the reflectivity of the mirrors by measuring the reflectivity as a function of wavelength at various mirror positions and corresponding angles, as presented in Sec. 4. By differentiating Bragg's law we see that $\Delta\theta = -(\Delta\lambda / \lambda)\tan\theta$. For the strictest case of Ni/B_4C/C multilayers for $\lambda = 4.6$ nm (Fig. 8a) we have $\Delta\lambda = 0.044$ nm at $\theta = 60°$, or $\Delta\theta = 0.9°$. In this case we have (Δx, Δy, Δz) = ±(0.5, 0.5, 1.8) mm. The tolerances at 13.5 nm wavelength are (Δx, Δy, Δz) = ±(1.6, 1.7, 6.4) mm.

Note that in its use in the FEL experiment, the mirror must be positioned so that the direct beam passes through the 0.6-mm-radius hole in the mirror. In practice, the center of the hole can be aligned to the FEL beam to better than 0.1 mm in *x* and *y* using a visible laser that is co-

aligned to the FEL beam. The tolerances of Eqns. (4) and (5) are the accuracy to which the coating coordinate system may be misaligned from the mirror hole coordinate.

Any tilt of the mirror, even within the tolerances described above, will result in a distortion of the diffraction pattern reflected on to the CCD. This distortion is equivalent to that caused by tilting the CCD by twice the amount so that it is no longer normal to the optic axis. Such a distortion may affect the image reconstruction since diffracted intensities will not be assigned to their correct spatial frequencies. In practice we find we can determine and correct for the error by measuring the locations of Bragg peaks in the diffraction pattern of a grid object. The largest distortion occurs at the edge of the CCD, and is given approximately by $(N/2)\sin 2\varepsilon \sin(\alpha + 2\varepsilon)$ pixels, for a tilt of the mirror by an angle ε, and where N is the width of the CCD in pixels. For example, for the N = 1340 pixel CCD, a tilt of the mirror by 0.5° causes a maximum distortion of less than 3 pixels. In practice we find no noticeable effect in the image reconstructions for distortions of this magnitude.

Scattering

An advantage of coherent diffractive imaging is that there is no lens that can distort or aberrate the image—the role of the lens is replaced by a computer algorithm which reconstructs an image from the diffraction pattern. However, as opposed to other similar experiments [23] we do have an optical element, the graded multilayer mirror, between the object and CCD detector. Ideally, this mirror should simply reflect the diffraction pattern on to the CCD without distorting or modifying the pattern in any way. Slope errors of no more than 0.1 mrad can easily be tolerated, as this would not cause rays to be deviated by more than half a pixel width, even for positions on the mirror furthest from the CCD. This level of surface flatness is easily achieved on commercial optical substrates.

A more difficult problem is that of roughness of the surface, which will lead to scattering of the diffracted light. Radiation scattered from the 45° mirror will be directed to the wrong pixel of the CCD, modifying the diffraction pattern of the specimen. This scattered light adds coherently to the diffraction pattern if the path difference between the scattered ray and a specularly reflected ray is less than the coherence length. Consider light scattering from a point on the mirror that is a distance a from the sample and a distance b from the CCD. We find that for a path difference Δ the scattering angle at the mirror approximately satisfies

$$\alpha^2 = 2\Delta\left(\frac{1}{a} - \frac{1}{b}\right) \qquad (7)$$

The coherence length can certainly be no longer than the pulse length, which for 30 fs duration, is about 10 μm. For points on the mirror closest to the CCD, we have b = 10 mm, which gives a largest scattering angle for coherent interference of α = 40 mrad. The angular extent of a 20 μm wide pixel at this distance is 2 mrad, so coherent interference could occur over a radius of 20 pixels. At larger scattering angles than 40 mrad the scattered light from the mirror will add an incoherent background to the pattern.

Both the coherent interference and incoherent background to the diffraction pattern is considered as noise that has to be minimized. In a multilayer structure, the roughness that causes scattering usually has two sources: the roughness of the substrate that is partly replicated throughout the multilayer structure, and the uncorrelated roughness that is generated by the deposition of each layer. The main task is to find deposition processes that minimize the roughness replication from layer to layer and produce a coating where the top layer is smoother than the best substrates. The efficiency of replication or smoothing depends of the spatial frequency or spatial period in the surface. High spatial frequencies are not replicated, while periods that are longer than 1 μm are nearly always completely replicated.

We can use the Debye-Waller factor as a first approximation to describe the influence of roughness on the performance of a mirror. The reduction in reflectivity is given by

$$R / R_0 = \exp\left\{-q^2\sigma^2\right\} = \exp\left\{-(\tfrac{4\pi\sigma}{\lambda} n\sin\theta)^2\right\} = \exp\left\{-(2\pi\sigma / d)^2\right\}, \qquad (8)$$

where σ is the roughness, q is the momentum transfer, represented by the wavelength and grazing angle of incidence θ, and d is the period of a multilayer that reflects at that wavelength and grazing angle. The roughness contains the contributions from different spatial periods, and for a range of scattering angles one has to choose the range of spatial periods that scatter into that angular range.

Fig. 3 is a plot of the normalized scattered intensity for two values of the mirror roughness as a function of the multilayer period obtained from Eq. (8) with the assumption that the loss in reflectivity appears as scattering. For normal incidence the multilayer period is about half the wavelength of the first order reflectivity maximum, for an angle of 45° the period is about 0.7 λ. We assumed a refractive index of 1 (one) for the plot. The value of σ = 0.2 nm corresponds to a typical coating produced by magnetron sputtering, and the value σ = 0.08 nm represents the smoothest coatings obtained up to now. Scattering is small for large wavelengths with correspondingly large multilayer periods but increases dramatically for shorter wavelengths. Table 1 lists in column 3 the expected total scattered intensity for a mirror used at 45° with a roughness value of σ = 0.2 nm. The fourth column is the measured angular acceptance (half-width at half-maximum) of the multilayer at a grazing angle of 60°, and the last column gives an estimate of the scattered intensity within that angle. For long wavelengths the amount of scattering is small, but mirror roughness will have to be reduced for the shorter wavelengths. If

we assume that 5% of scattering is acceptable than the smoothest coating made up to now (σ = 0.08 nm) would allow multilayer periods down to 2.5 nm, or a wavelength down to 3.5 nm at 45°.

We obtain the roughness of our mirror surfaces from AFM measurements. Figure 4 is a plot of the power spectral density (PSD) obtained for the mirror fabricated for λ = 32 nm. The roughness is obtained by integrating the PSD over the relevant spatial frequencies using

$$\sigma^2 = 2\pi \int_{f_1}^{f_2} PSD(f)\, f df \,. \tag{9}$$

The detector in our experiment (Fig. 1) collects scattered radiation from the mirror within an acceptance angle of 26°. The vertical line in Fig. 4 represents the spatial frequency that corresponds to that angle for λ = 32 nm. The roughness of σ = 0.16 nm is obtained by including only the frequencies below that line.

4. Multilayer coatings at various wavelengths

Optics for 32 nm

In our first experiments at FLASH we used mirrors operating at 32 nm [24]. Among possible multilayer designs we considered Mo/Si [25], Mg/SiC [26,27], Si/B_4C [28] and Si/C [29] multilayers. Our requirements for high multilayer stability favored multilayers with Si, B_4C and C materials, due to their high melting temperatures. At the time of the first FLASH experiments (January 2005) little was known about Mg/SiC multilayer stability, although a later publication [30] shows that Mg/SiC has good stability up to 200ºC. We arrived with the final

multilayer design (Si/Mo/B_4C) based on two additional criteria. One was related to the high stress of Si/B_4C multilayer and stress variation across the mirror due to large period variation, and the other was a desire to have a multilayer with a wide reflectivity peak width due to the uncertainty in the FLASH wavelength at the early stage of its operation. In addition, it has been calculated theoretically [31], and also demonstrated experimentally [32], that for these longer wavelengths where absorption is high a third material in the multilayer structure substantially increases the reflectivity. The multilayer unit structure we developed for 30-32 nm consists of three materials, Si/Mo/B_4C, as counted from the substrate up [24]. The relative thicknesses of Mo, Si and B_4C were optimized using the IMD [33] software. In order to reduce the force due to stress we minimized the number of tri-layer units to 10. This had another positive effect, an increase in the bandwidth of the reflectivity peak. All layer thicknesses were smoothly graded from one end of the optic to the other with layer thicknesses from 11.4/0.35/0.56 nm (Si/Mo/B_4C) for 60° incidence angle (zero angle is at grazing incidence) to 18.4/0.75/0.84 for 30°. These values do not take into account the period thickness contraction due to interface formation. The intrinsic stress for the 60° design was 1450 MPa (compressive) and 1140 MPa (compressive) for 30°. The smallest grazing angles (close to 30° incidence angle) of the coating approached the region of total internal reflection of a single boundary where the required multilayer period becomes very large. We restricted the change in period of our multilayer design to a factor of two and succeeded to produce coatings with a smooth reflectivity change in the transition region between multilayer and total reflection based contributions. (See Fig. 5a)

To deposit the Si/Mo/B_4C multilayer, three sputtering targets, Si, Mo and B_4C mounted on the bottom of the sputtering chamber, were utilized simultaneously. All the coatings were deposited at 1 mTorr. In general, the larger the sputtering target area the easier it is to control the

deposition rate profile across the substrate. The Si and B_4C targets were rectangular (127 × 254 mm) while Mo was a 100-mm diameter round target. The power on the Mo target was 50 W, on Si 360W, and on B_4C 400W.

Before coating, the glass substrates were characterized for their surface roughness with Atomic Force Microscope (AFM) and showed a level of high-spatial-frequency roughness between 0.19 and 0.21 nm rms. Coated mirrors were characterized at the Advanced Light Source (ALS) [20] at Lawrence Berkeley National Laboratory and some of them were also measured at the National Synchrotron Light Source (NSLS) at Brookhaven National Laboratory and the SURF facility at National Institute of Standards and Technology. Figure 5a shows experimental data on an example mirror, displaying reflectivity curves $R(\lambda)$ for many mirror positions r at the required incidence angle. Figure 5b shows the reflectivity at the design wavelength λ = 31 nm and the design incidence angle. The zero (low) reflectivity near r = 25 mm corresponds to the hole in the mirror. We observe no loss in reflectivity due to slightly higher substrate roughness (0.2 nm rms) of our optic as compared to a multilayer deposited on a super-polished Si wafer substrate with only 0.1 nm rms high spatial frequency roughness. This is not surprising since substrate roughness and scattering are less detrimental at longer wavelengths. The multilayer mirror with 10 repeats of Si/Mo/B_4C reflects at 31 nm from 33% (at 60° incidence angle) to 43% (30° incidence angle), respectively showing a smooth transition to the total reflection range where the incidence angle is smaller than the critical angle of the terminating Si layer.

The reflectivity curves at 31-nm wavelength are very broad, making this mirror quite insensitive to misalignments as discussed in Sec. 3. In particular, for the 60° reflection we have a half width at half reflectivity of $\Delta\lambda$ = 3.4 nm, or $\Delta\theta$ = 10°. The alignment tolerances of the mirror, given by Eqns. (4)-(6) are (Δx, Δy, Δz) = ± (5.4, 5.6, 21) mm.

Optics for 16 nm

Graded multilayer coatings for a wavelength of 16 nm were tested with the second harmonic of FLASH. As with the 32 nm optic we required a broad bandwidth of ~20% due to the uncertainty of the wavelength. Our design consists of 30 repeats of $Si/B_4C/Mo$ with Si deposited on the substrate first and Mo last. A reflectivity between 41% and 50% across the mirror was achieved at 16.0 nm wavelength.

The pulse energy of the second harmonic is less than 0.3% of the first harmonic, so an efficient discrimination of 16 nm from 32 nm was required. This was achieved with a combination of a Xe-filled 15-m long gas-cell attenuator [34] (which transmitted 10% at 32 nm and 90% at 16 nm) and an antireflective coating. A reflectivity ratio of 0.002:1 for 16 nm : 32 nm was achieved by depositing an antireflective layer directly on the multilayer stack to suppress the reflection of the 1st harmonic (32 nm) without noticeable loss in reflectivity at 16 nm. This consisted of a 43-nm layer of silicon, which reduced the reflectivity at 32 nm to <<1% over the whole acceptance angle range, as shown in Figure 6, while keeping 16-nm reflectivity above 40%.

At the 60° incidence angle the half width at half reflectivity is $\Delta\lambda = 0.5$ nm, or $\Delta\theta = 3.5°$. The alignment tolerances of the mirror in this case, given by Eqns. (4)-(6) are $(\Delta x, \Delta y, \Delta z) = \pm$ (1.7, 1.8, 6.8) mm.

Optics for 13.5 nm

For 13.5 nm wavelength we deposited 35 bilayers of a Mo/Si multilayer. The mirror reflectivity varied between 65% (60° incidence angle) and 66% (30°) as shown in Figure 7a. As discussed in Sec. 3, the alignment tolerances of this optic, which has a half-width at half

maximum angular acceptance of 3.3° is (Δx, Δy, Δz) = ±(1.6, 1.7, 6.4) mm. The uniform performance at 13.5 nm across the mirror is shown in Figure 7b.

Optics for 4.5 nm

We also developed 45° mirrors for a wavelength of 4.5 nm (3rd harmonic of 13.5 nm). This coating consisted of Ni/B_4C/C. Pure Ni/C multilayers, with periods between 2.6 and 4.6 nm, had much lower reflectivity than predicted due to discontinuous layers of Ni. We studied this phenomenon, first observed by Spiller [35], in more detail. Two effects suggest this reflectivity reduction is due to interface roughness: lower reflectivity and an increase in high spatial frequency roughness with an increasing number of layers beyond 60 [24]. The reflectivity should increase with the number of bilayers, N, but we observe decrease in reflectivity for $N > 60$. Normal incidence reflectivity of up to 1% was achieved with 60 bilayer Ni/C multilayers. However, by adding a thin layer of B_4C on C-on-Ni interface we demonstrated a substantial reflectivity increase [24]. Over 7% normal incidence reflectivity was measured on 60 bilayer Ni/B_4C/C multilayers with 0.9 nm thick B_4C interface layers (Figures 8a and 8b). For B_4C interlayers thicker than 0.9 nm the benefit of interface smoothing effect is suppressed by the higher absorption of B_4C compared with C. Better performance is expected with Co/C multilayers because Co and C have larger difference in refractive index and absorption as compared to Ni and C.

This wavelength, which has a multilayer acceptance half angle of $\Delta\theta = 0.9°$ is the most stringent for alignment and the transfer of coordinates between the fabrication, characterization, and experimental systems. As discussed in Sec. 3, the positional tolerance for this mirror are (Δx, Δy, Δz) = ±(0.5, 0.5, 1.8) mm.

5. Diffraction measurements

An example of a single-pulse coherent diffraction pattern measured at FLASH with the mirror-based camera is shown in Fig. 9a, recorded with the 1340 × 1300 pixel CCD. In this case no absorber was placed between the mirror and CCD. The object consisted of a pattern milled by focused-ion beam into a 20-nm thick membrane of silicon nitride that is supported over a 20-μm wide square aperture in a silicon wafer. The wavelength was 32 nm, the pulse energy was 10±3 μJ, or $(1.6\pm0.5)\times10^{12}$ photons, and the pulse duration was approximately 30 fs. The intensity of the diffraction pattern is displayed with a logarithmic grey-scale. It is evident that the pattern has a high degree of contrast, which indicates that the amount of incoherent stray light (e.g. from high-angle scattering from the mirror, scattering from beamline components, or plasma radiation from the exploding sample) is minimal. The diffraction pattern was created by an object consisting of a regular array of holes, giving rise to the array of strong peaks in the pattern. We choose this particular pattern for illustration of the operation of the camera as we can easily observe the overall uniformity of the mirror response across the pattern. For the binary object that was used here the diffraction pattern should be centrosymmetric. In fact, by comparing the intensities of pairs of peaks reflected about the origin, there is a slight gradient in reflectivity that is consistent with the measurement of Fig. 5b. Additionally, the performance of the mirror hole is apparent from the diffraction pattern. Even though intense scattering from the object extends to the edge of the mirror hole (particularly the strong horizontal and vertical cross bars, which are caused by diffraction from the edges of the square aperture in which the sample is located), this light is not strongly scattered by the hole edge. This is because the reflectivity of the mirror diminishes gradually towards the hole edge and so there are no hard edges to scatter from. The reduction in reflectivity is caused by surface roughness near the hole. Also, because

the mirror surface tends to tilt in towards the hole, the light reflected from this region is directed in towards the shadow of the hole, as can faintly be seen. This light is masked out of the pattern prior to image retrieval.

Another indication of the quality of the diffraction pattern is that it could be easily phased to form the real-space image shown in Fig. 9b. This reconstruction was carried out by the Shrinkwrap algorithm [36], after first correcting for the reflectivity gradient shown in Fig. 5b. The image shown is an average of 50 reconstructions from independent initial starts of the algorithm, which represents the best estimate of the object [2]. No prior knowledge about the object was used in the reconstruction, and the pattern of dots agrees with the hole-pattern created by the focused-ion beam. The image explains the features of the diffraction pattern: the regular Bragg peaks in the pattern were caused by the array of holes, and the intensity pattern laid down on each peak is given by the Fourier transform of the overall shape of the dot array. In the vertical direction between neighbouring Bragg peaks there are 10 satellite peaks, caused by the interference between the horizontal edges of the object (which are 10 dot spacings apart). The entire diffraction pattern is modulated by the Fourier transform of the shape of the dots. Due to astigmatism of the focused ion beam the dots (actually holes in the membrane) are slightly elliptical. The Fourier transform of these elliptical holes is an elliptical Airy-like pattern, noticeable as the dark ring between the second and third diffraction order in the vertical direction and at the third diffraction order in the horizontal direction.

The low spatial frequencies of the object are lost to the hole in the mirror. These missing frequencies extend out to about the second satellite peak in the vertical, which in real space would correspond to two periods between the horizontal edges (or modulations of periods of five dot spacings and longer). However, in this case, the shape transform is repeated at the Bragg

peaks, and essentially the only information that is missing is the strength of the zero-order Bragg peak which gives the overall scattering strength of the object. In more general non-periodic objects the degree of missing information depends on the shape of the object [37]. It may be possible in the future to measure the missing low spatial frequencies on a detector placed many metres downstream of the camera, where the diverging beam will have expanded enough that a second detector (or attenuator) can survive the pulses.

Other examples of single-pulse coherent diffraction patterns and holograms recorded with the camera have been published elsewhere [3,17].

6. Summary

We have developed, constructed, and tested a camera to record coherent scattering patterns with a soft-X-ray FEL. The camera is based on a novel laterally-graded multilayer mirror that reflects the scattering pattern onto a bare CCD. The mirror acts as a bandpass filter both for wavelength and angle, and is tailored so that rays of the correct wavelength emanating only from a volume centered on the sample reflect to the CCD. The mirror solves the particular problem of the extreme intensity of the pulses, which are focused to greater than 10^{14} W/cm^2 and which create a plasma from all materials placed in the 20-μm focus. The strong undiffracted pulse passes through a hole in the mirror and propagates on to a beam dump rather than interacting with a beamstop placed near the CCD. Our results prove the robustness and sensitivity of the camera, and we have recorded over 30,000 diffraction patterns with this configuration.

The geometry of the mirror has proven to be very flexible. Besides the ability to record diffraction patterns with high sensitivity and reduced noise from stray light or plasma radiation, the camera can be configured to record patterns at high scattering angles, and in a backscattering

geometry. The multilayer mirror coating must be chosen for a particular wavelength, and we have fabricated mirrors for 32 nm (Si/Mo/B_4C), 16 nm (Si/B_4C/Mo with an anti-reflective coating for 32 nm), 13.5 nm (Mo/Si), and 4.5 nm (Ni/B_4C/C). Mirrors for other wavelengths can be manufactured, although fabrication becomes more difficult, and tolerances become tighter, as the wavelength is reduced. However, the concept will certainly be applicable for the full range of the fundamental wavelength of the FLASH FEL and at other soft-X-ray FELs under consideration (i.e. between 4 nm and 60 nm) and could also be applied into the water window [38] between the carbon and oxygen *K*-shell absorption edges. The technology of steeply-graded multilayer optics demonstrated here opens up a wide range of experiments at FEL and other soft-X-ray sources, such as stereo imaging, and time-resolved two-color pump-probe experiments.

Acknowledgments

We would like to thank T. Möller and C. Borstedt (TU Berlin) for accommodating our experiment in their chamber. We would also like to acknowledge S. Ayers, R. Hill, S. Baker, J. C. Robinson, and R. Levesque (LLNL), A. Aquila, F. Dollar and E. M. Gullikson (LBNL), B. Kjornrattanawanich (NSLS), C. Tarrio, S. Grantham, T. Lucatorto (NIST) for their technical contributions and support. We thank the FLASH staff at DESY, ALS staff at Lawrence Berkeley National Laboratory, NSLS staff at Brookhaven National Laboratory and SURF staff at NIST for facilitating the experiments. This work was performed under the auspices of the U.S. Department of Energy by Lawrence Livermore National Laboratory under contract DE-AC52-07NA27344; the U.S. Department of Energy Office of Science to the Stanford Linear Accelerator Center, the Swedish Research Council and the Swedish Foundation for International Cooperation in Research and Higher Education (SFB and JH).

Tables

λ (nm)	*d* (nm)	I_{sc} (%)	$\Delta\theta$ (°) at 60°	I_{sc} (%) in $\Delta\theta$ at 60°
32	24	0.31	9.75	0.25
16	12	1.1	6.3	1.3
13.5	10.1	1.5	2.1	1.0
6.7	5.0	6.1	1.26	5.0
4.5	3.3	13.5	1.2	12

Table 1. Normalized total scattered intensity I_{sc} calculated for a roughness σ = 0.2 nm for a 45° mirror used at the wavelengths λ. *d* is the period of a multilayer that reflects at that wavelength and angle. The fourth column is the measured angular acceptance (half-width at half-maximum) of the multilayer at a grazing angle of 60°, and the last column gives an estimate of the scattered intensity within that angle. A straight line fit of the PSD in Fig. 4 towards low spatial frequencies was used for this estimate. In all cases the lowest spatial frequency f_1 =0.005 nm^{-1} was used in the integration of eq. (9) while f_2 is obtained from the scattering angle in column 4.

Figure captions

Figure 1: Schematic of the camera setup. The FEL pulse is incident from the left and intersects the sample, located at *S*. Scattered rays reflect from the multilayer-coated mirror onto a filtered CCD detector. The coating is rotationally symmetric about the axis *SO*. A block prevents scattered rays from directly hitting the CCD.

Figure 2: Schematic of the shadow mask to deposit the desired profile $d(r)$ on an optical substrate. The grey region is opaque and the white region is open. The origin of the coordinate system corresponds to $r = 0$ in Fig. 1. The substrate and a witness sample are mounted off-axis in a mount that spins about the point $r = 0$. The deposited thickness $d(r)$ is proportional to the angular extent of the open area, depicted for two values of r.

Fig. 3. Fraction of the reflected intensity at a boundary that appears as scattering for different roughness and different multilayer periods.

Fig. 4. Measured Power Spectral Density (PSD) of the Si/Mo/B_4C mirror used at $\lambda = 32$ nm. The top scale gives the corresponding scattering angle around the 45° incidence angle. Only spatial frequencies below the vertical line contribute to scattering within 26° from specular, the acceptance angle of the detector for scattered radiation, producing a roughness of 0.16 nm, while the total roughness is 0.34 nm.

Figure 5: Line-scan of reflectivity as a function of wavelength along the 45° mirror. Bottom dashed line is reflectivity curve at 60° incidence angle and the top dashed line is reflectivity

curve for 30° incidence angle (which is in the total reflection regime). The plot on the right shows extracted reflectivity values at 31 nm as a function of distance on the mirror. The low reflectivity values correspond to the hole in the middle of the mirror.

Figure 6: Reflectivity curves for different angles on the mirror showing high reflectivity at 16 nm and suppression at 32 nm.

Figure 7: Reflectivity as a function of wavelength along the 45° mirror. Bottom dashed line is reflectivity curve at 60° incidence angle and the top dashed line is reflectivity curve for 30° incidence angle (which is in the total reflection regime). The low reflectivity values near the 25 mm position correspond to the hole in the middle of the mirror. Reflectivity across the 45° mirror at 13.5 nm.

Figure 8: Multilayer mirror reflecting at 4.6 nm

Fig. 9. Diffraction pattern (a) and reconstruction (b).

References

1. K. J. Gaffney and H. N. Chapman, “Imaging atomic structure and dynamics with ultrafast x-ray scattering,” Science **316**, 1444-1448 (2007).
2. D. Shapiro, P. Thibault, T. Beetz, V. Elser, M. Howells, C. Jacobsen, J. Kirz, E. Lima, H. Miao, A. M. Neiman, D. Sayre, “Biological imaging by soft x-ray diffraction microscopy,” Proc. Natl. Acad. Sci. USA **102**, 15343-15346 (2005).
3. H. N. Chapman, A. Barty, M. J. Bogan, S. Boutet, M. Frank, S. P. Hau-Riege, S. Marchesini, B. W. Woods, S. Bajt, H. Benner, R. A. London, E. Plonjes, M. Kuhlmann, R. Treusch, S. Dusterer, T. Tschentscher, J. R. Schneider, E. Spiller, T. Moller, C. Bostedt, M. Hoener, D. A. Shapiro, K. O. Hodgson, D.Van der Spoel, F. Burmeister, M. Bergh, C. Caleman, G. Huldt, M. M. Seibert, F. R. N. C. Maia, R. W. Lee, A. Szoke, N. Timneanu, J. Hajdu, "Femtosecond diffractive imaging with a soft-X-ray free-electron laser," Nat. Phys. **2**, 839-843 (2006).
4. W. Chao, B. D. Harteneck, J. A. Liddle, E. H. Anderson, and D. T. Attwood, “Soft x-ray microscopy at a spatial resolution better than 15 nm,” Science **435**, 1210–1213 (2005).
5. D. Sayre, H. N. Chapman, and J. Miao. “On the extendibility of x-ray crystallography to noncrystals,” Acta Cryst. A **54**, 232–239 (1998).
6. J. Miao, P. Charalambous, J. Kirz, and D. Sayre, “Extending the methodology of x-ray crystallography to allow imaging of micrometre-sized non-crystalline specimens,” Nature **400**, 342–344 (1999).
7. G. J. Williams, M. A. Pfeifer, I. A. Vartanyants, and I. K. Robinson, “Three-dimensional imaging of microstructure in Au nanocrystals,” Phys. Rev. Lett. **90**, 175501 (2003).

8. H. N. Chapman, A. Barty, S. Marchesini, A. Noy, S. P. Hau-Riege, C. Cui, M. R. Howells, R. Rosen, H. He, J. C. H. Spence, U. Weierstall, T. Beetz, C. Jacobsen, and D. Shapiro, "High-resolution ab initio three-dimensional x-ray diffraction microscopy," J. Opt. Soc. Am. A **23**, 1179–1200 (2006).
9. G. W. Stroke, *An Introduction to Coherent Optics and Holography*, Academic, New York (1969).
10. I. McNulty, J. Kirz, C. Jacobsen, E. H. Anderson, M. R. Howells, and D. P. Kern, "High-Resolution Imaging by Fourier Transform X-ray Holography," Science **256**, 1009–1012 (1992).
11. S. Eisebitt, J. Luning, W. F. Schlotter, M. Lorgen, O. Hellwig, W. Eberhardt, and J. Stohr., "Lensless imaging of magnetic nanostructures by x-ray spectro-holography," Nature **432**, 885–888 (2004).
12. R. Neutze, R. Wouts, D. van der Spoel, E. Weckert, and J. Hajdu, "Potential for biomolecular imaging with femtoscond X-ray pulses," Nature **406**, 752-757 (2000).
13. J. R. Fienup, "Phase retrieval algorithms—a comparison," Appl. Opt. **21**, 2758–2769 (1982).
14. S. Marchesini, H. He, H. N. Chapman, S. P. Hau-Riege, A. Noy, M. R. Howells, U. Weierstall, J. C. H. Spence, "X-ray image reconstruction from a diffraction pattern alone," Phys. Rev. B **68**, 140101, (2003).
15. M. Howells, C. Jacobsen, S. Marchesini, S. Miller, J. Spence, and U. Weirstall, "Toward a practical X-ray Fourier holography at high resolution," Nucl. Instrum. Meth. A **467** 864–867 (2001).
16. W. Ackermann, G. Asova, V. Ayvazyan, A. Azima, N. Baboi, J. Bähr, V. Balandin, B. Beutner, A. Brandt, A. Bolzmann, R. Brinkmann, O. I. Brovko, M. Castellano, P. Castro, L.

Catani, E. Chiadroni, S. Choroba, A. Cianchi, J. T. Costello, D. Cubaynes, J. Dardis, W. Decking, H. Delsim-Hashemi, A. Delserieys, G. Di Pirro, M. Dohlus, S. Düsterer, A. Eckhardt, H. T. Edwards, B. Faatz, J. Feldhaus, K. Flöttmann, J. Frisch, L. Fröhlich, T. Garvey, U. Gensch, Ch. Gerth, M. Görler, N. Golubeva, H.-J. Grabosch, M. Grecki, O. Grimm, K. Hacker, U. Hahn, J. H. Han, K. Honkavaara, T. Hott, M. Hüning, Y. Ivanisenko, E. Jaeschke, W. Jalmuzna, T. Jezynski, R. Kammering, V. Katalev, K. Kavanagh, E. T. Kennedy, S. Khodyachykh, K. Klose, V. Kocharyan, M. Körfer, M. Kollewe, W. Koprek, S. Korepanov, D. Kostin, M. Krassilnikov, G. Kube, M. Kuhlmann, C. L. S. Lewis, L. Lilje, T. Limberg, D. Lipka, F. Löhl, H. Luna, M. Luong, M. Martins, M. Meyer, P. Michelato, V. Miltchev, W. D. Möller, L. Monaco, W. F. O. Müller, O. Napieralski, O. Napoly, P. Nicolosi, D. Nölle, T. Nuñez, A. Oppelt, C. Pagani, R. Paparella, N. Pchalek, J. Pedregosa-Gutierrez, B. Petersen, B. Petrosyan, G. Petrosyan, L. Petrosyan, J. Pflüger, E. Plönjes, L. Poletto, K. Pozniak, E. Prat, D. Proch, P. Pucyk, P. Radcliffe, H. Redlin, K. Rehlich, M. Richter, M. Roehrs, J. Roensch, R. Romaniuk, M. Ross, J. Rossbach, V. Rybnikov, M. Sachwitz, E. L. Saldin, W. Sandner, H. Schlarb, B. Schmidt, M. Schmitz, P. Schmüser, J. R. Schneider, E. A. Schneidmiller, S. Schnepp, S. Schreiber, M. Seidel, D. Sertore, A. V. Shabunov, C. Simon, S. Simrock, E. Sombrowski, A. A. Sorokin, P. Spanknebel, R. Spesyvtsev, L. Staykov, B. Steffen, F. Stephan, F. Stulle, H. Thom, K. Tiedtke, M. Tischer, S. Toleikis, R. Treusch, D. Trines, I. Tsakov, E. Vogel, T. Weiland, H. Weise, M. Wellhöfer, M. Wendt, I. Will, A. Winter, K. Wittenburg, W. Wurth, P. Yeates, M. V. Yurkov, I. Zagorodnov & K. Zapfe, “Operation of a free-electron laser from the extreme ultraviolet to the water window,” Nature Phot. **1**, 336–342 (2007).

17. H. N. Chapman, S. P. Hau-Riege, M. J. Bogan, S. Bajt, A. Barty, S. Boutet, S. Marchesini, M. Frank, B. W. Woods, W. H. Benner, R. A. London, U. Rohner, A. Szöke, E. Spiller, T. Möller, C. Bostedt, D. A. Shapiro, M. Kuhlmann, R. Treusch, E. Plönjes, F. Burmeister, M. Bergh, C. Caleman, G. Huldt, M. Marvin Seibert, J. Hajdu, "Femtosecond time-delay X-ray holography," Nature **448**, 676-679 (2007).

18. M. J. Bogan, W. H. Benner, S. Boutet, U. Rohner, M. Frank, M. Seibert, F. Maia, A. Barty, S. Bajt, V. Riot, B. Woods, S. Marchesini, S. P. Hau-Riege, M. Svenda, E. Marklund, E. Spiller, A. Szoke, J. Hajdu, and H. N. Chapman, "Singe particle x-ray diffractive imaging," 2007, in preparation.

19. E. Spiller, *Soft X-Ray Optics*, SPIE, Bellingham WA (1994).

20. J. H. Underwood, and E. M. Gullikson, "High-resolution, high-flux, user friendly VLS beamline at the ALS for the 50-1300 eV energy region," J. Electron Spectrosc. Relat. Phenom. **92**, 265-272 (1998).

21. S. Bajt, R. D. Behymer, P. B. Mirkarimi, C. Montcalm, M. A. Wall, M. Wedowski, and J. A. Folta, "Experimental investigation of beryllium-based multilayer coatings for extreme ultraviolet lithography," SPIE Proc. **3767**, 259-270 (1999).

22. R. Soufli, R. M. Hudyma, E. Spiller, E. M. Gullikson, M. A. Schmidt, J. C. Robinson, S. L. Baker, C. C. Walton, J. S. Taylor, "Sub-diffraction-limited multilayer coatings for the 0.3 numerical aperture micro-exposure tool for extreme ultraviolet lithography," Appl. Opt. **46**, 3736-3746 (2007).

23. T. Beetz, M. Howells, C. Jacobsen, C. Kao, J. Kirz, E. Lima, T. Mentes, H. Miao, C. Sanchez-Hanke, D. Sayre, and D. Shapiro, "Apparatus for x-ray diffraction microscopy and tomography of cryo specimens," Nucl. Instrum. Meth. A **545**, 459–468 (2005).

24. S. Bajt, H. N. Chapman, E. Spiller, S. Hau-Riege, J. Alameda, A. J. Nelson, C. C. Walton, B. Kjornrattanawanich, A. Aquila, F. Dollar, E. Gullikson, C. Tarrio, S. Grantham, "Multilayers for next generation x-ray sources," SPIE Proc. **6586**, 6586-18 (2007).

25. K. Yamashita, S. Takahashi, S. Kitamoto, S. Takahama, K. Tamura, I. Hatsukade, M. Sakurai, M. Watanabe, A. Yamaguchi, H. Nagata and M. Ohtani, "Characterization of multilayer reflectors and position sensitive detectors in the 45-300 Å region," Rev. Sci. Instrum. **63**, 1513-1515 (1992).

26. Y. Kondo, T. Ejima, K. Saito, T. Hatano, M. Watanabe, "High-reflection multilayer for wavelength range of 200–30 nm," NIM A **467-468**, 333-336 (2001).

27. I. Yoshikawa, T. Murachi, H. Takenaka S. Icimaru, "Multilayer coating for 30.4 nm," Rev. Sci. Instrum. **76**, 066109 (2005).

28. J. M. Slaughter, B. S. Medower, R. N. Watts, C. Tarrio, T. B. Lucatorto, C. M. Falco, "Si/B_4C narrow-bandpass mirrors for the extreme ultraviolet," Opt. Lett. **19**, 1786-1788 (1994).

29. M. Grigonis, and E. J. Knystautas, "C/Si multilayer mirrors for the 25-30 nm wavelength region," Appl. Opt. **36**, 2839-2842 (1997).

30. T. Ejima, A. Yamazaki, T. Banse, K. Saito, Y. Kondo, S. Ichimaru, and H. Takenaka, "Aging and thermal stability of Mg-SiC and Mg-Y_2O_3 reflection multilayers in the 25–35 nm region," Appl. Opt. **44**, 5446- 5453 (2005).

31. J. I. Larruquert, "Reflectance enhancement in the extreme ultraviolet and soft x rays by means of multilayers with more than two materials," J. Opt. Soc. Am. **A 19,** 391-397 (2002).

32. J. Gautier, F. Delmotte, M. Roulliay, F. Bridou, M.-F. Ravet, and A. Jérome, "Study of normal incidence of three-component multilayer mirrors in the range 20-40 nm," Appl. Opt. **44**, 384-390 (2005).

33. D. L. Windt, "IMD - Software for modeling the optical properties of multilayer films," Computers in Physics **12**, 360-370 (1998).

34. U. Hahn and K. Tiedtke, "The gas attenuator of FLASH at DESY," AIP Conference Proc. **879**, 276–282 (2007).

35. E. Spiller and K.-B. Youn, "Studies towards optimization of ion polishing for multilayer x-ray mirrors," SPIE Proc. **2011**, 288-298 (1993).

36. S. Marchesini, H. He, H. N. Chapman, S. P. Hau-Riege, A. Noy, M. R. Howells, U. Weierstall, and J. C. H. Spence, "X-ray image reconstruction from a diffraction pattern alone," Phys. Rev. B **68**, 140101 (2003).

37. P. Thibault, V. Elser, C. Jacobsen, D. Shapiro, and D. Sayre, "Reconstruction of a yeast cell from x-ray diffraction data," Acta Cryst. A **62**, 248–261 (2006).

38. see http://www-cxro.lbl.gov (reflectivity results by F. Salmassi and E. M. Gullikson).

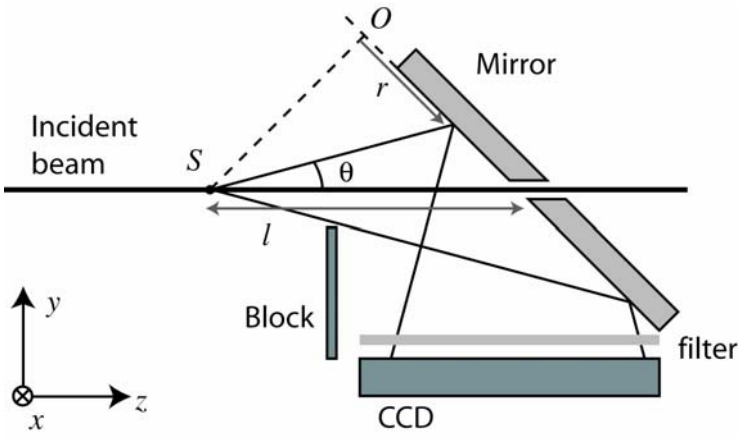

Figure1

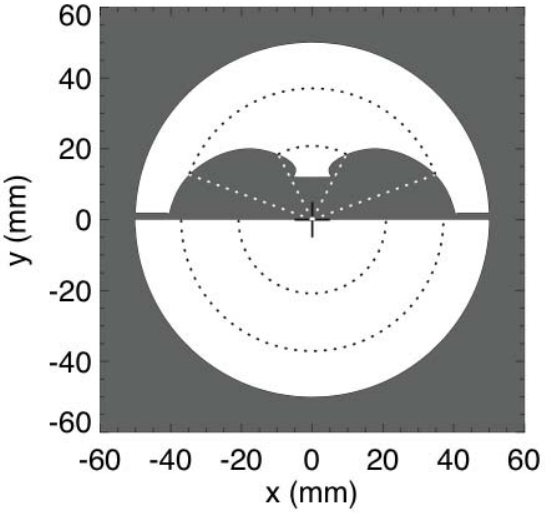

Figure 2

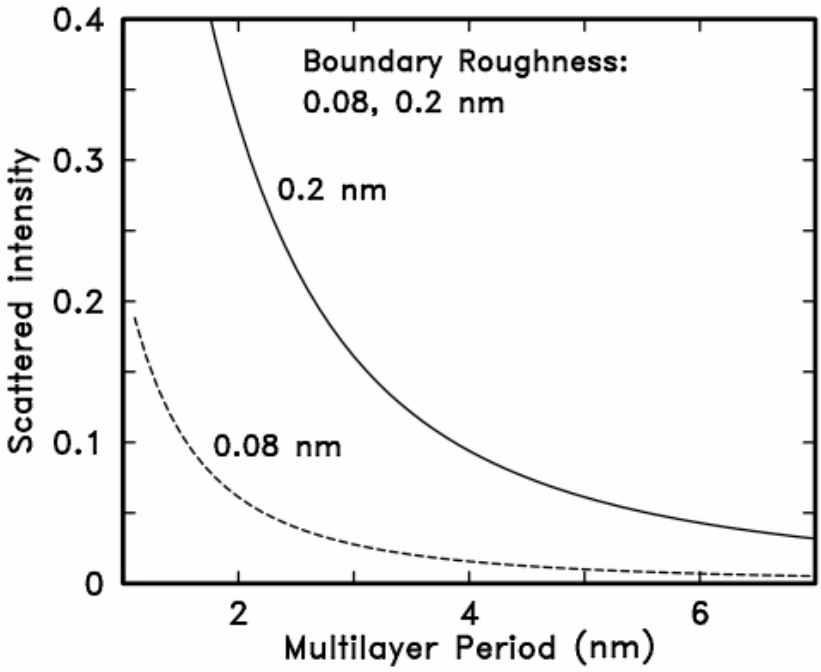
0.4
0.3
0.2
0.1
0
Scattered intensity
Boundary Roughness:
0.08, 0.2 nm
0.2 nm
0.08 nm
2
4
6
Multilayer Period (nm)

Figure 3

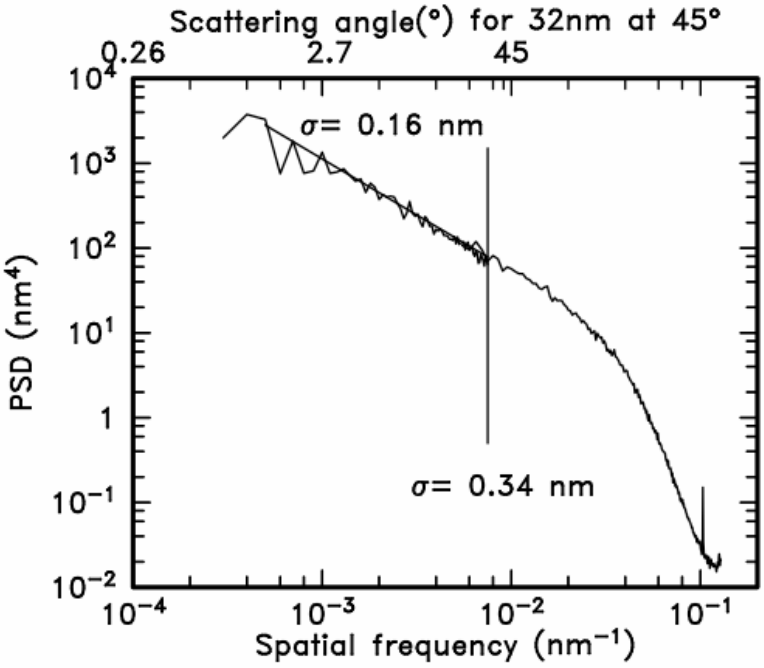
Scattering angle(°) for 32nm at 45°
0.26
2.7
45
σ= 0.16 nm
σ= 0.34 nm
PSD (nm⁴)
Spatial frequency (nm⁻¹)

Figure 4

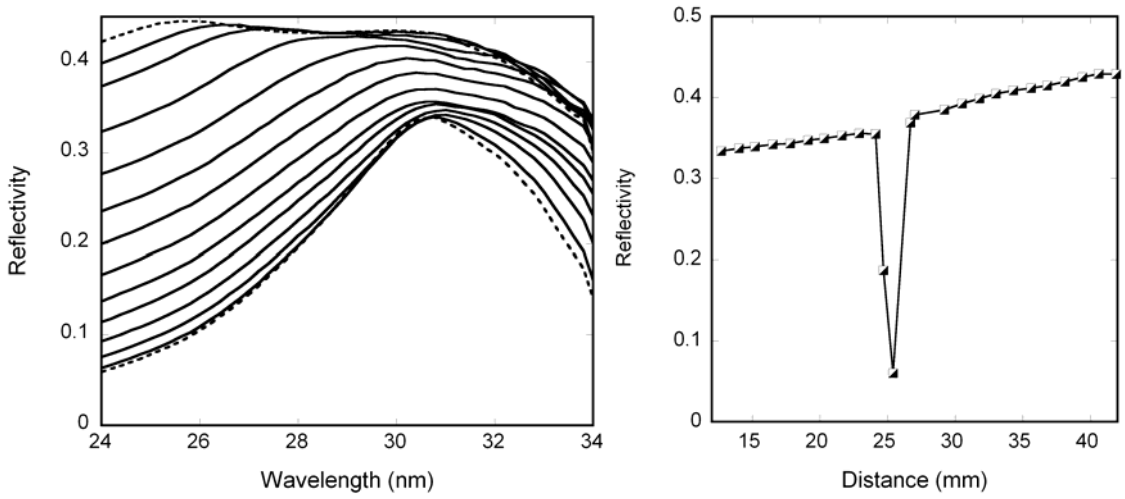

Figures 5a and 5b

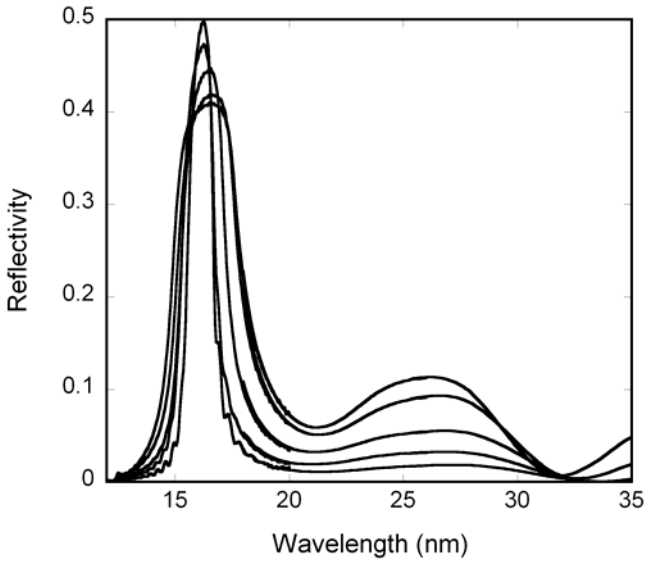

Figure 6

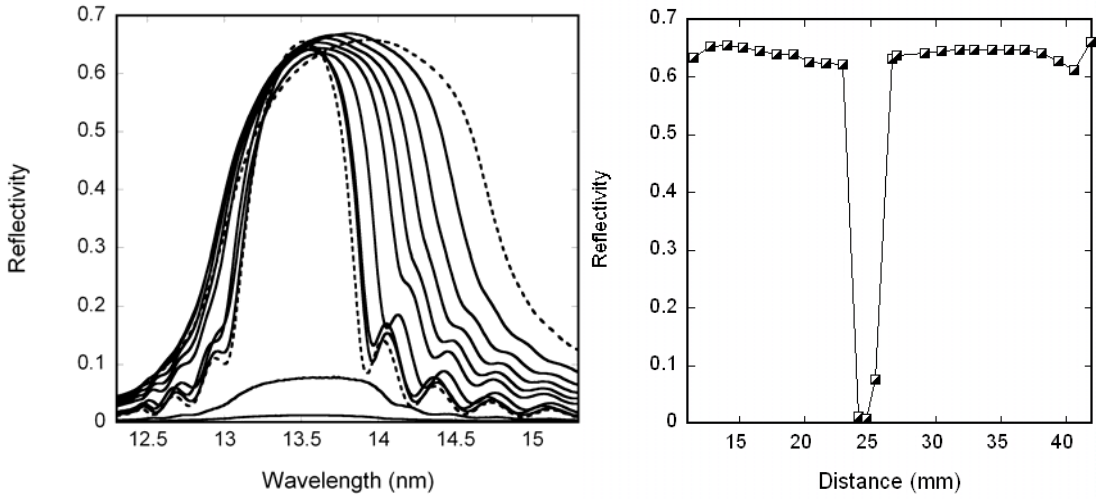

Figure 7a and 7b

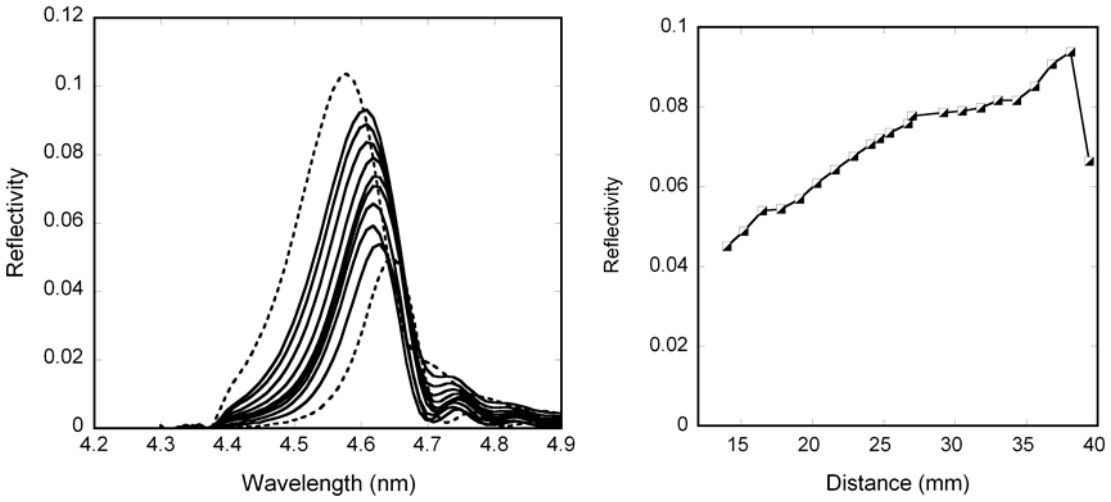

Figure 8a and 8b

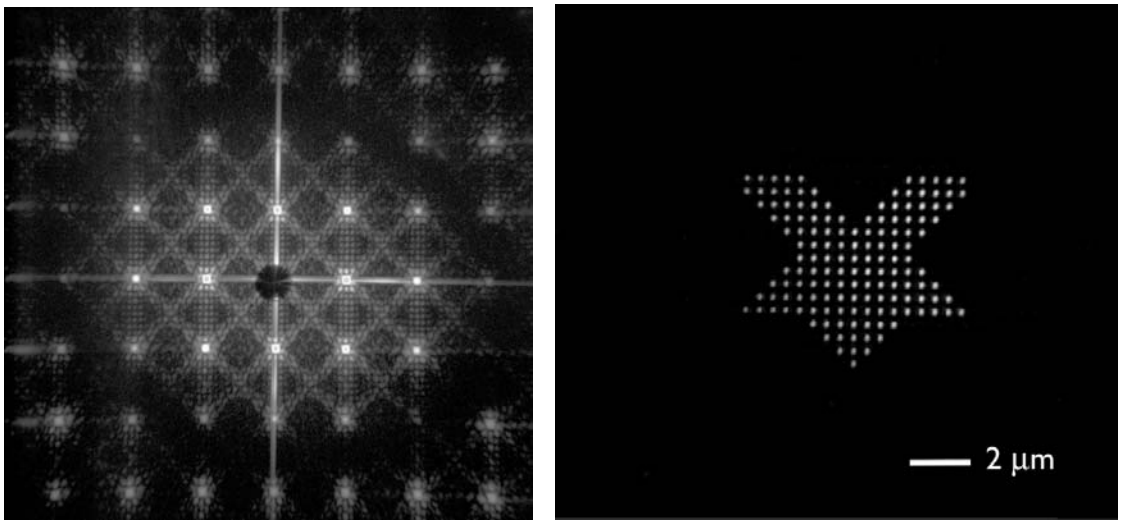

Figure 9a and 9b